Chapter One

Introduction and Motivation

1.1 THE FIELD OF HIGH-ENERGY ASTROPHYSICS

Compared with optical astronomy, which traces its foundations to prehistoric times,[1] the field of high-energy astrophysics is a relatively new science, dealing with astronomical sources and phenomena largely discovered since the advent of space-based instrumentation.[2] Ironically, however, the earliest signs of high-energy activity from space appeared in laboratory equipment on the ground, and were not recognized as extraterrestrial for many years.

Physicists had noted since about 1900 that some unknown ionizing radiation had to be present near Earth's surface, from the manner in which the leaves of an electroscope always came together, presumably as a result of a gradual discharging. By 1912, Victor Hess (1883–1964) had made several manned balloon ascents to measure the ionization of the atmosphere as a function of altitude, making the surprising discovery[3] that the average ionization above $\sim$1.5 km increased relative to that at sea level. By demonstrating in this manner that the source of the ionizing radiation—named *cosmic rays* by Robert Millikan (1868–1953) in 1925—must therefore be extraterrestrial, Hess opened up the frontier of high-energy astrophysics and was eventually awarded the Nobel prize in physics in 1936.

Not long after World War II, the ready availability of sounding rockets facilitated the first major discovery of the high-energy sources themselves. The name *sounding rocket* comes from the nautical term "to take a sounding," meaning to make a measurement. Typically consisting of a solid-fuel rocket motor and a payload, these devices are commonly used to carry instruments and to take readings from about 50 to 1500 km above Earth's surface, between the regions sampled by weather balloons and orbiting satellites. The sounding rocket consumes its fuel during the rising portion of the flight, then the payload separates to complete the arc and land on the ground with a parachute. Data are collected for up to 15 min at a time while the payload is flying ballistically above Earth's atmosphere.

The first scientific flight of a sounding rocket in 1949 carried a photon (Geiger) counter and showed unambiguously that the Sun emits X-rays.[4] Not long after

[1] See, e.g., Ruggles and Saunders (1993).

[2] We will learn shortly in this chapter why high-energy observations must be made above Earth's atmosphere.

[3] Hess's balloon flights reached as high as 5 km above sea level. One of his followers, Kolhörster, ascended to 9 km a few years later. See Hess (1912).

[4] See Friedman, Lichtman, and Byram (1951).

that, in 1962, Riccardo Giacconi and colleagues carried out another sounding rocket experiment that many consider to be the birth of X-ray astronomy.[5] Though flown to investigate X-rays from the moon, the 1962 experiment instead discovered Sco X-1, the brightest X-ray source in the sky, and with it, a completely unexpected diffuse glow of X-rays coming from all directions—the cosmic X-ray background.

Experimental and observational astronomy have grown rapidly since then, with the numbers and size of detection systems increasing steadily with satellites in the 1970s, to a broadening international effort in the 1980s, to even larger and more imposing spacecraft in the 1990s and beyond. Today, high-energy instrumentation is being developed and deployed not only by the United States, but also by countries in Europe, member states of the former Soviet Union, Asia, and South America.

But though much of what we have learned about the ultraviolet (UV), X-ray, and γ-ray sky has occurred in space, we should not come away with the thought that high-energy astrophysics is *exclusively* a space-based discipline. From the beginning, high-altitude balloons could carry heavy payloads of larger aperture for flights lasting $\sim$10 h or more, at altitudes of $\sim$40 km. As we shall see, only X-rays exceeding $\sim$20 keV in energy can penetrate down this far in the atmosphere, but to this day, balloon experiments continue to provide important observational results in the 20- to 60-keV portion of the spectrum.

At even higher energies, the atmosphere itself becomes part of the detector, providing a target for the highest energy photons as they descend from space, thereby producing a cascade of particles and radiation that reach Earth's surface. Thus, at TeV energies and higher (where $1\,\mathrm{TeV} = 10^{12}\,\mathrm{eV}$), observational high-energy astronomy is actually best conducted from the ground. Early in the 21st century, some of the most spectacular gains in this field have been made by air Cerenkov telescopes, as they are known, and we will consider these in detail, along with other detector techniques, later in this chapter.

Regardless of the photon energy, however, the principal feature that distinguishes high-energy astrophysics from other branches of astronomy is the relative paucity of photons in the X-ray and γ-ray bands. Instrument builders must factor this into their designs. Several years ago, the National Aeronautics and Space Administration (NASA) in the United States was seriously considering funding the development of a detector, to be attached to the international space station, that would collect a scant 300–500 photons over its entire two-year lifetime.

There are at least two reasons why this occurs. First, the energy of the photons precludes large numbers of them being emitted concurrently. A 1-MeV γ-ray carries as much energy as one million optical photons, so for a given (limited) energy budget, it is a lot more difficult to produce high-energy γ-rays than photons detected by optical means. Second, the sky is far less crowded in X-rays and γ-rays than

[5]Giacconi's extensive work in high-energy astrophysics was recognized with the awarding of the Nobel prize in physics in 2002, "for pioneering contributions to astrophysics, which have led to the discovery of cosmic X-ray sources." The results from the 1962 sounding-rocket flight were reported in Giacconi et al. (1962).

in other spectral regimes. One can actually count the high-energy point sources. Indeed, until very recently, all of them could be assigned individual names.[6]

Given the complexity of building and deploying these detectors, experimental high-energy astrophysics now tends to be what physicists would call a "big science." As in particle physics, nothing meaningful can be done anymore without the strong participation of a large group of collaborators, often at several different universities and government laboratories. In high-energy astrophysics, this effort must also be supplemented by the key participation of one or more space agencies, such as NASA in the United States and the European Space Agency (ESA).

High-energy astrophysics is also an important theoretical discipline, encompassing many other sub-branches of physics. Broadly speaking, high-energy astrophysics involves the study of (1) large quantities of energy, usually coupled to relativistic matter, (2) the rapid release of this energy in events of extreme violence, sometimes completely destroying the underlying source, (3) the interaction of matter and radiation under the extreme conditions of superstrong gravity and magnetic fields, and (4) the emission of large fluxes of X-rays, γ-rays, and sometimes also UV radiation.

Although interesting as an instrumental and observational science, high-energy astrophysics is therefore also particularly attractive to theoreticians because it provides new physical problems and tests of fundamental theories, such as general relativity, under conditions that are totally inaccessible in the laboratory, or even within the solar system. Consider this: one teaspoonful of neutron-star material weighs as much as all of humanity combined. And a marshmallow dropped onto the surface of that neutron star releases enough gravitational energy to produce an explosion equal to that of a medium-sized atomic bomb on Earth. This is the realm of physical reality we will be exploring in this book.

1.2 ENERGIES, LUMINOSITIES, AND TIMESCALES

Before we move on to consider the hurdles one must face in first building high-energy telescopes and then using them effectively to interrogate the electromagnetic signals reaching Earth from distant high-energy sources, let us orient ourselves by considering several characteristic scales. For example, it matters when building a device to measure variability in the source whether the emitter changes its profile over a period of several microseconds or much more slowly over an interval of many months.

As we develop the theoretical tools used in high-energy astrophysics throughout this book, we will encounter a variety of particle acceleration mechanisms, each scaled by its own critical energy and fiducial acceleration time. The simplest to consider is gravity, so we will here estimate certain critical numbers characterizing the high-energy emission by compact objects accreting from their environment.

The release of gravitational potential energy by matter falling onto a compact object is believed to be the principal source of power in sources as diverse as the

[6]As we shall see later in this chapter, the most dramatic change in our view of the X-ray sky occurred when the satellite ROSAT was deployed in the early 1990s. Within the first six months of operation, ROSAT produced a catalog exceeding 100,000 X-ray sources.

accreting star in a low-mass X-ray binary and the significantly more powerful and distant supermassive black hole in active galactic nuclei (AGNs) and quasars.

A mass m falling onto an object of (bigger) mass M and radius R releases a quantity of energy

$$\Delta E_{\rm acc} = \frac{GMm}{R}. \tag{1.1}$$

Thus, for a neutron star with mass $M_{\rm ns} \sim 1 M_\odot$ and radius $R_{\rm ns} \approx 10\,{\rm km}$ (the size of a typical city),

$$\Delta E_{\rm acc}({\rm ns}) \approx 10^{20}\,{\rm ergs\,g^{-1}}. \tag{1.2}$$

As we shall see, on a neutron star this energy eventually emerges in the form of X-rays and γ-rays. By comparison, hydrogen burning into helium releases a quantity of energy

$$\Delta E_{\rm nuc}({\rm H} \rightarrow {\rm He}) \approx 6 \times 10^{18}\,{\rm ergs\,g^{-1}}, \tag{1.3}$$

so the accretion yield for a neutron star is about 20 times bigger than the process we commonly associate with the release of energy in main sequence stars (hence the "doomsday" marshmallow anecdote from before).

These numbers, however, are not universal since $\Delta E_{\rm acc}$ depends on the compactness M/R of the accreting object. For example, a white dwarf also has a mass $M_{\rm wd} \sim 1 M_\odot$, but a radius $R_{\rm wd}$ ($\sim 10^9$ cm) about equal to that of Earth. For such an object, M/R is so small that

$$\Delta E_{\rm acc}({\rm wd}) \approx \tfrac{1}{50}\,\Delta E_{\rm nuc}({\rm H} \rightarrow {\rm He}). \tag{1.4}$$

On the other hand, black holes have a characteristic radius $R_S = 2GM/c^2$, the event (or Schwarzschild) horizon to be defined in chapter 3. For them, $M/R \sim c^2/2G$, and

$$\Delta E_{\rm acc}({\rm bh}) \approx 5 \times 10^{20}\,{\rm ergs\,g^{-1}}. \tag{1.5}$$

Black holes do not have a hard surface (like a neutron star or a white dwarf) so we do not expect all of the energy released gravitationally to be observable as electromagnetic radiation, since some of it is presumably advected through the horizon.

There are at least two additional questions we should ask about the energy released by gravity. First, what is the total luminosity (or power) associated with such a process? Second, how quickly can the emission region vary? Knowing the luminosity of a typical high-energy source permits us to infer its energy flux arriving at Earth, and hence the required instrument sensitivity to measure it. These days, analyzing the timing behavior of an astronomical source can be just as informative as studying its spectral characteristics, so, as we have already indicated, we must also have an idea of the source's variability.

To address the first of these, let us suppose that we have a fully ionized hydrogen gas accreting isotropically onto a compact star. Aside from the effects of a magnetic (or perhaps even an electric) field, there are generally two forces on the plasma,

one arising from the inward pull of gravity, and a second (an outward force) due to Thomson scattering between the charged particles in the gas and the radiated photons diffusing outward. It is the balance between these two influences that sets the luminosity scale.

Although both electrons and protons are present in the infalling plasma, the outward force is dominated by scatterings between the photons and electrons. Thomson scattering by protons is much less important due to their significantly smaller cross section. To understand this in a heuristic manner, let us think of the scattering classically as a one-dimensional process, in which the charge behaves as an oscillator responding to an electric wave $\mathbf{E}(z, t)$ passing through the medium in the $\hat{\mathbf{z}}$-direction. From Newton's law

$$\frac{d\mathbf{p}}{dt} = q\mathbf{E}, \tag{1.6}$$

where $\mathbf{p}$ is the particle's momentum and q is its charge. For a harmonic wave

$$\mathbf{E}(z, t) = E_0(z)e^{i\omega t}\,\hat{\mathbf{x}}, \tag{1.7}$$

the particle's (one-dimensional) equation of motion reads

$$m\frac{d^2x}{dt^2} = qE_0(z)e^{i\omega t}. \tag{1.8}$$

The solution to this differential equation is trivial, and may be written in the form

$$x(t) = -Ae^{i\omega t}, \tag{1.9}$$

where A is the amplitude of the motion, given by the expression

$$mA\omega^2 = qE_0(z), \tag{1.10}$$

or more simply as

$$A = \frac{qE_0(z)}{m\omega^2}. \tag{1.11}$$

Evidently, the amplitude of the charge's oscillation is inversely proportional to its mass, and the cross-sectional area, which is roughly proportional to A^2, will therefore go as $\sim m^{-2}$. So labeling the proton and electron Thomson cross sections as σ_{Tp} and σ_{Te}, respectively, we infer that

$$\frac{\sigma_{Tp}}{\sigma_{Te}} = \left(\frac{m_e}{m_p}\right)^2 \approx 3 \times 10^{-7}. \tag{1.12}$$

The actual value of this ratio, here deduced classically, should not be taken too literally. However, we will use the large disparity between σ_{Tp} and σ_{Te} to justify our assumption that only electron Thomson scattering needs to be considered in calculating the outward radiation force on the infalling plasma.

Within the plasma, therefore, the gravitational force is stronger for the protons, these being the more massive particles, whereas the outward radiative force is greater for the electrons, these having the bigger cross section. But the two particle species do not separate spatially since the Coulomb attraction between them prevents this

from happening. For the purpose of finding the force balance, it suits us to think of the ionized gas as comprising loosely coupled electron–proton pairs, even though in the ionized state, the two oppositely charged sets of particles are more like two fluids passing through each other. The gravitational force on each couplet is then simply

$$f_{\rm grav} = -\frac{GM\,(m_p + m_e)}{r^2}. \tag{1.13}$$

To find the corresponding force $f_{\rm rad}$ due to Thomson scattering, we must consider the rate of momentum transfer from the outwardly streaming radiation to the electrons in the plasma. As we shall see in chapter 3, a photon of energy ϵ carries a momentum ϵ/c, so radiation with energy flux F (in units of energy per unit area per unit time) also carries a momentum flux

$$\Pi = \frac{F}{c}. \tag{1.14}$$

The radiative force on the electron in each couplet is the momentum per unit time transferred to it from Π. Henceforth denoting σ_{Te} as simply σ_T, we therefore have

$$f_{\rm rad} = \frac{F}{c}\sigma_T. \tag{1.15}$$

For an isotropic point source of radiation with luminosity L, this can also be written

$$f_{\rm rad} = \frac{\sigma_T\, L}{4\pi c r^2}, \tag{1.16}$$

and so the net force on the particle couplet is

$$f_{\rm grav} + f_{\rm rad} = \left[-GM\,(m_p + m_e) + \frac{\sigma_T\, L}{4\pi c}\right]\frac{1}{r^2}. \tag{1.17}$$

When the two forces appearing on the left-hand side of equation (1.17) are equal (and opposite), the right-hand side of this equation must, of course, vanish. The critical luminosity for which this occurs is known as the Eddington limit (or luminosity). Since $m_p \gg m_e$, one simply puts $m_p + m_e \approx m_p$, which gives

$$L_{\rm edd} \equiv \frac{4\pi c GM m_p}{\sigma_T}. \tag{1.18}$$

Numerically, we have

$$L_{\rm edd} \approx 1.3 \times 10^{38}\left(\frac{M}{M_\odot}\right)\ {\rm ergs\,s^{-1}}. \tag{1.19}$$

Thus, the Eddington luminosity for a neutron star with mass $M_{\rm ns} = 1.4\,M_\odot$ is $\sim 10^4\,L_\odot$ (all in X-rays, as we shall see shortly), whereas for an AGN black hole with mass $M_{\rm AGN} = 10^7\,M_\odot$, the Eddington luminosity is $\sim 10^{45}$ ergs s^{-1}, roughly 10 times the luminosity of the entire galaxy.

The Eddington limit is an important characteristic luminosity because sources with $L > L_{\rm edd}$ expel nearby matter and quench the process of accretion. For this reason, the Eddington luminosity is a reliable measure of the power expected from a very active source of mass M, deriving its energy by absorbing matter from its environment.

For compact objects, this power is usually manifested as UV photons or X-rays, though sometimes secondary processes may recycle this radiation to yet higher energies. The effective temperature $T_{\rm eff}$ of a blackbody radiating a total power $L_{\rm edd}$ is given by

$$4\pi R^2 \sigma_B T_{\rm eff}^4 = L_{\rm edd}, \tag{1.20}$$

where σ_B is the Boltzmann constant. With equation (1.18), this gives

$$T_{\rm eff} = \left(\frac{cGMm_p}{R^2 \sigma_T \sigma_B} \right)^{1/4}. \tag{1.21}$$

Thus, for a neutron star, $T_{\rm eff}\,({\rm ns}) \approx 2 \times 10^7$ K, corresponding to a characteristic photon energy $h\nu = kT_{\rm eff} \approx 1.6$ keV (X-rays). White dwarfs, on the other hand, emit with an effective temperature $T_{\rm eff}\,({\rm wd}) \approx 6 \times 10^5$ K, with characteristic photon energy ≈ 50 eV (UV). In the case of a black hole, the spectrum cannot be interpreted without understanding the accretion process more fully, since the absence of a hard surface means that most of the gravitational energy is released over an extended region of space.

We are now in a position to estimate the photon counting rate required of our detectors in order to measure, say, the X-ray flux reaching us from a typical neutron star near the center of our Galaxy. The photon number flux impinging on Earth's atmosphere from one of these sources is roughly $F_{\rm ph} \equiv L_{\rm edd}/4\pi D^2 \langle \epsilon \rangle$, where D ($\approx$8.5 kpc) is the distance to the galactic center and $\langle \epsilon \rangle$ ($\sim$1.6 keV) is the average photon energy. Thus, $F_{\rm ph} \sim 10\,{\rm ph\,cm^{-2}\,s^{-1}}$. By comparison, the very first X-ray orbital mission in 1970, named *Uhuru*, achieved a limiting sensitivity of $\sim 6 \times 10^{-3}\,{\rm ph\,cm^{-2}\,s^{-1}}$, rendering such neutron-star sources easily detectable over the mission lifetime. The *Chandra* observatory (see section 1.5), one of the most recently deployed X-ray satellites, achieves a sensitivity of about $2 \times 10^{-6}\,{\rm ph\,cm^{-2}\,s^{-1}}$ in 10^5 seconds of integration, greatly enhancing our capability of discovering very faint sources, many of which accrete well below the Eddington limit.

The second question we posed with regard to the transfer of energy from gravity to the radiating plasma concerns the variability timescale $t_{\rm var}$ in the emitting region. For gravity, $t_{\rm var}$ is heavily influenced by the dynamical timescale $t_{\rm dyn}$, which we estimate as follows.

Consider an element of mass m falling under the influence of gravity above the surface of a star. An upper limit to $t_{\rm var}$ is the time it takes for m to fall a distance R, the star's radius. Let us put

$$\tfrac{1}{2} a t_{\rm dyn}^2 \equiv R, \tag{1.22}$$

where $a = GM/R^2$ is the gravitational acceleration. Rewriting this in the form

$$t_{\rm dyn} = \left(\frac{2R^3}{GM} \right)^{1/2}, \tag{1.23}$$

we find that $t_{\rm dyn}\,({\rm ns}) = 10^{-4}$ s for a neutron star. Similarly, for a white dwarf we estimate that $t_{\rm dyn}\,({\rm wd}) = 3$ s. For a black hole, the situation is again unclear without a more complete understanding of the emitter's geometry, particularly since jets are

often important—if not dominant—contributors to the overall emission from these objects. Doppler shifts and light-travel time effects, which we will develop later in this book, can seriously modify the variability timescale inferred by a distant observer relative to what is actually taking place in the emitter's frame. Observationally, we already know that some AGNs, like the BL Lac object H 0323+022, display variability in all wavebands, including the X-ray,[7] where the source varies on a timescale as short as $\sim$30 s. That is surprising considering the fact that the light-travel time ($\sim 2R_S/c$) around a black hole with mass $\sim 10^8\, M_\odot$ is about half an hour, which is the shortest interval one would think of associating with the local dynamical time. So clearly some other effect, probably due to relativistic length contraction, is at play in transforming the variability timescale in the emitter's frame into that measured by the observer.

Our instruments will detect changes in the emitter's configuration only if they can accumulate reasonable photon counting statistics to measure the incoming flux from typical high-energy sources in several seconds; the integration time needs to be even shorter—only a fraction of a millisecond—in the case of neutron stars. As we shall see later in this chapter, the high-energy observatories built thus far have tended to specialize in either imaging capability or spectral energy resolution, though only with a modest ability to resolve the source temporally. The one exception has been the *Rossi* X-ray Timing Explorer, launched in December 1995, whose remarkable temporal resolution has allowed astronomers to resolve changes occurring over only a fraction of a millisecond in the brightest objects.

1.3 ATMOSPHERIC ABSORPTION

We next familiarize ourselves with the difficulties faced by experimental high-energy astrophysicists in constructing X-ray and γ-ray detectors that, with appropriate deployment, can sense the radiation reaching us from astronomical sources. Their triumph in overcoming nature's hurdles has been recognized by the Nobel prize committee, which has thus far awarded two prizes in this field.[8]

There is a very good reason why our eyes have developed the greatest sensitivity to light in the $\sim$400- to 700-nm range of wavelengths—the aptly labeled "visible" portion of the spectrum. Without this capability, the long development of optical astronomy since prehistoric times would have been impossible. This waveband not only encompasses most of the Sun's spectral output—roughly a blackbody peaking at a wavelength of $\sim$600 nm, right in the middle of this range—but also represents one of the few regions in the spectrum where atmospheric absorption is virtually nonexistent. These two factors mean that most of the light reaching us from our environment has a wavelength between 400 and 700 nm. Conversely, the intensity of light at many

[7] See Feigelson et al. (1986).

[8] As noted earlier in this chapter, Victor Hess was the first recipient, in 1936, for discovering cosmic rays. Riccardo Giacconi received his award in 2002 for his life's work in essentially creating the field of X-ray astronomy.

other wavelengths is severely attenuated near Earth's surface. In a way, this is actually a good thing as far as our survival is concerned, given that UV, X-ray, and γ-ray photons tend to seriously damage our cells. Unfortunately, the atmosphere's effective absorption of radiation at wavelengths shorter than the visible also strongly mitigates any possibility of viewing cosmic high-energy radiation directly from the ground, even up to the TeV range, where what we see are the secondary particles produced by collisions between the extraterrestrial photons and the upper atmosphere.

Photons can interact with atmospheric particles in several ways. Below about 60 keV (i.e., for wavelengths $\lambda \gtrsim 2 \times 10^{-9}$ cm, or 0.2Å), the dominant interaction is the photoelectric effect, in which an atomic electron completely absorbs the incident photon and is ejected. As such, the cross section for this process increases sharply at the so-called absorption edges, where the photon energy is sufficient to knock out an electron in the next (deeper) energy level. In the simplest description of radiation transfer through a medium with density ρ, the attenuation suffered by a ray with intensity I (in units of ergs cm^{-2} s^{-1} ster^{-1}) is described according to the differential equation

$$\frac{dI}{ds} = -\mu\rho I, \tag{1.24}$$

where the absorption coefficient μ is defined as the cross section per unit mass of the material, and s is the pathlength. If the medium is uniform, equation (1.24) integrates easily and the solution is

$$I(d) = I_0 \exp(-\mu\rho d), \tag{1.25}$$

where d is the distance into the medium, or simply its thickness if the ray has penetrated all the way through. Figure 1.1 shows the mass absorption coefficient μ as a function of photon energy for three elements—silicon, chlorine, and iron—in which the absorption edges are clearly visible. The larger the value of μ is, the shorter is the distance d required for a photon at this energy to be absorbed.

Above $\sim$10 MeV, photons passing through the atmosphere begin to produce electron–positron pairs. An individual photon traveling through vacuum cannot spontaneously materialize in this fashion because, as we shall see in chapter 3, its energy–momentum relation is not the same as that of particles with a nonzero rest mass. A single photon splitting into an electron–positron pair therefore cannot simultaneously conserve both energy and momentum. Within the Coulomb field of another charge, however, such as the nucleus of an atom or ion, this process is physically permitted because the incoming photon can interact with a virtual photon while their center of momentum moves subluminally in the observer's frame.[9] The absorption coefficient κ for this process is also straightforward to write down from QED, though we will here only show the results graphically (see figure 1.2 below).

Between these two energies (i.e., between $\sim$60 keV and $\sim$10 MeV), the dominant interaction suffered by extraterrestrial radiation in Earth's atmosphere is inelastic

[9]The first individuals to consider this process, Landau and Lifshitz, have written extensively on this subject, including the book *Quantum Electrodynamics*, a volume in their highly regarded series on theoretical physics. See Landau and Lifshitz (1982).

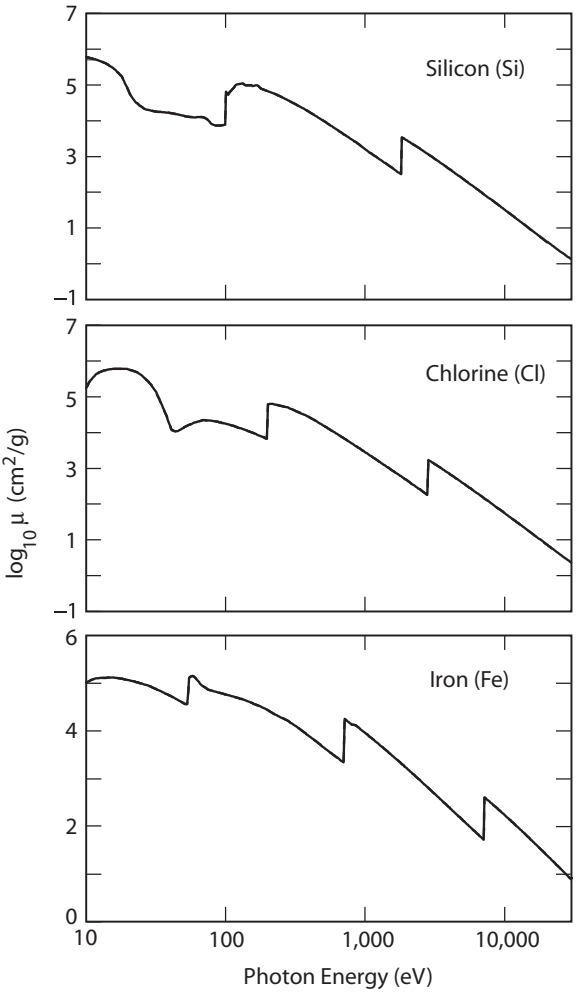

Figure 1.1 Mass absorption coefficients for silicon, chlorine, and iron as functions of energy. The absorption coefficient is dominated by photoabsorption over most of the energy range 10 eV to 30 keV. As discussed in the text, μ is related to the intensity I transmitted through a material density ρ and thickness d by $I = I_0 \exp(-\mu\rho d)$, where I_0 is the entering intensity. (Based on data from Henke, Gullikson, and Davis 1993)

Compton scattering, where the incoming photon scatters with a free electron and transfers a fraction of its energy to it. In cosmic-ray astronomy, it is common to separate the Compton scattering coefficient σ_c into two parts, the coefficient σ_a representing the energy absorbed by the particles, and σ_s representing the scattered photon energy. What really counts as far as attenuation is concerned, however, is the total coefficient

$$\sigma_c = \sigma_a + \sigma_s, \tag{1.26}$$

where

$$\sigma_a \equiv \sigma_c \frac{\langle \Delta\epsilon \rangle}{\epsilon} \tag{1.27}$$

and

$$\sigma_s = \sigma_c \left(1 - \frac{\langle \Delta\epsilon \rangle}{\epsilon}\right). \tag{1.28}$$

In these expressions, $\langle \Delta\epsilon \rangle$ is the average energy lost by an incoming photon with energy ϵ once it scatters with the medium.[10]

Figure 1.2 shows the total attenuation coefficient μ_0 for photons propagating through air, given as

$$\mu_0 = \mu_a + \sigma_s, \tag{1.29}$$

where μ_a is the total absorption coefficient defined as

$$\mu_a \equiv \tau + \sigma_a + \kappa. \tag{1.30}$$

The coefficient for Rayleigh scattering, labeled σ_r in this figure, drops precipitously with increasing energy and may be ignored in high-energy astronomy.

Returning now to equation (1.25), we see that for a significant fraction of the incoming intensity I to survive down to a certain distance d in the atmosphere, the "optical depth" $\mu\rho d$ must be of order one or less. Therefore, the main conclusion we draw from figure 1.2 is that for photon energies $\epsilon \gtrsim 0.5\,\mathrm{MeV}$, astronomical measurements must be made at column densities $\rho d \lesssim 1/\mu_0 \sim 10\,\mathrm{g\ cm^{-2}}$ into the atmosphere, since $\mu_0 \lesssim 0.1\,\mathrm{cm^2\ g^{-1}}$ at these energies. On Earth, this atmospheric column density corresponds to a height of approximately 30 km above sea level (see figure 1.3), and for this reason, high-energy astrophysics is primarily a high-altitude and space-based scientific discipline.

The exercise we have just carried out for photon energies $\epsilon \gtrsim 0.5\,\mathrm{MeV}$ can be extended over the entire spectrum, from radio to ultra high-energy γ-rays, and the result can be represented graphically as shown in figure 1.4. This diagram shows the penetration depth of extraterrestrial photons descending to a level above the ground where the attenuation factor in equation (1.25) drops below $1/e$. Radio waves have no trouble reaching Earth's surface, though absorption by the humidity in the atmosphere for wavelengths shorter than $\sim 0.5\,\mathrm{mm}$ is as efficient as any of the other absorptive processes we discussed earlier. The visible band is quite clean, but at UV energies and higher, virtually all of the incoming intensity is absorbed well above the ground. We will see shortly how these natural constraints can be overcome to provide astronomers with the tools they need to observe extraterrestrial high-energy sources.

[10]Be aware that the symbol σ is more commonly used to represent a cross section whose units are simply area. The quantities σ_c, σ_a, and σ_s, with units of area per unit mass, are employed in cosmic-ray astronomy. We will emphasize the difference whenever any possible confusion may arise.

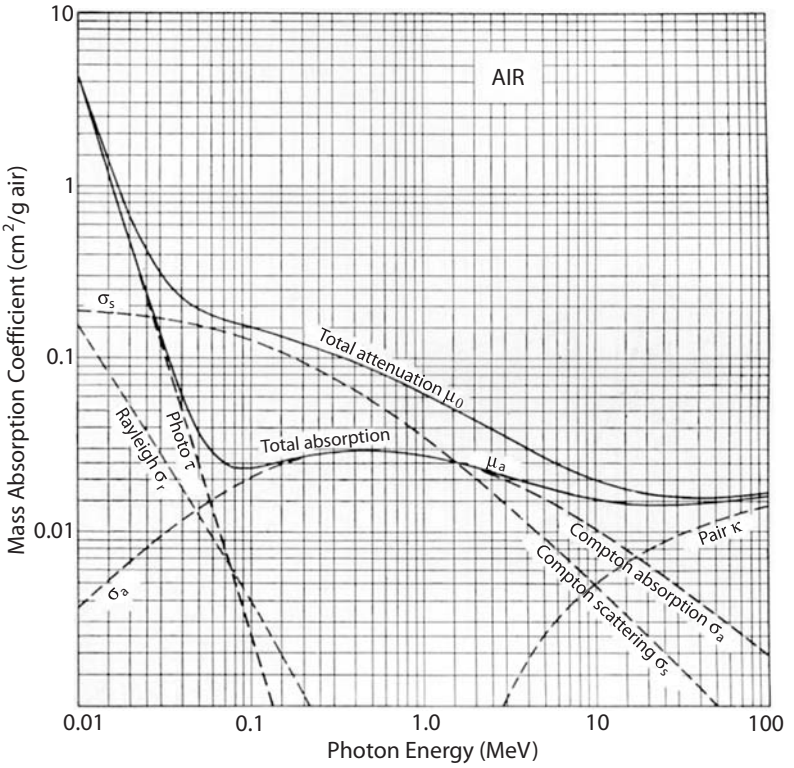

Figure 1.2 Mass absorption coefficients for photons in air. The labeled curves correspond to Compton absorption (σ_a), Compton scattering (σ_s), photoelectric absorption (τ), pair production (κ), and Rayleigh scattering (σ_r), which is elastic and confined to small angles, and can usually be ignored at the energies shown here. The curve marked "total absorption" shows the sum $\tau + \sigma_a + \kappa$. Adding Compton scattering to this yields the "total attenuation" coefficient μ_0. The composition for air in this diagram is 78.04 volume percent nitrogen, 21.02 volume percent oxygen, and 0.94 volume percent argon. (From Evans 1955)

1.4 EXPERIMENTAL TOOLS OF HIGH-ENERGY ASTROPHYSICS

Besides deploying our detector judiciously above most of Earth's atmosphere, we must also deal with at least two other challenges that loom in high-energy astronomy, requiring technological developments beyond the extensive instrumentation already available at longer wavelengths. One of these is the development of methods to focus high-energy radiation onto the detector, and the second is the design of the detectors themselves. High-energy photons penetrate much deeper into matter than their longer wavelength counterparts and are therefore difficult to reflect (and refract). At the highest energies, γ-rays are also very destructive, both to themselves and to the material they encounter. Before we discuss high-energy telescopes, we therefore need to first consider the physics of collecting and analyzing photons in the UV to TeV energy range.

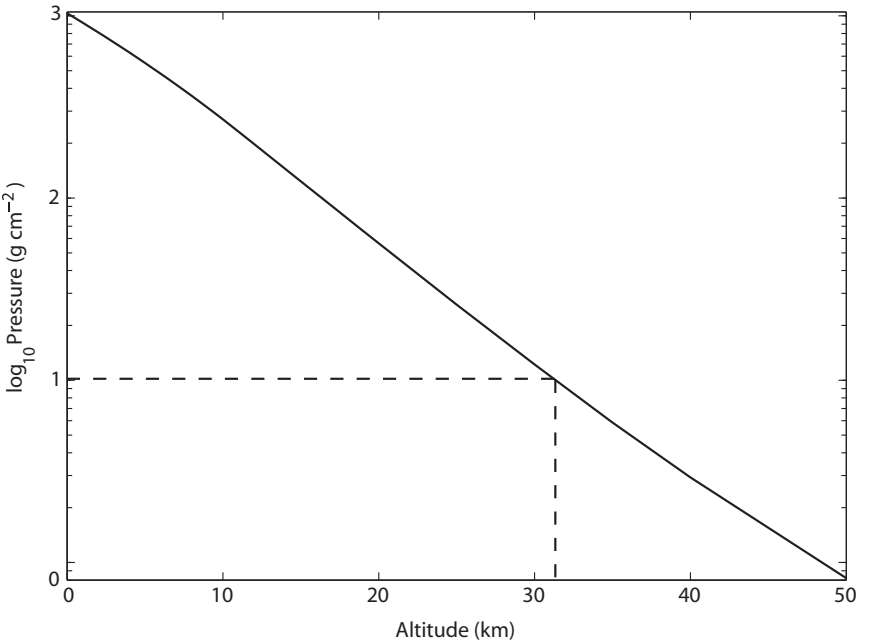

Figure 1.3 Atmospheric pressure (actually represented here as a column density of air in units of g cm^{-2}) as a function of altitude (in km) above Earth's surface. The pressure drops to a value below $\sim$10 g cm^{-2} only for heights above $\sim$30 km. (Based on the atmospheric model of Arguado and Burt 1999)

Modern UV and soft X-ray observatories use charge-coupled devices (CCDs) to capture incoming photons. A CCD is an array of (usually) silicon or germanium pixel elements with bias voltages that make each of them a small potential well. The incident photon ejects an electron that remains trapped in the well until the array is read out by a single low-noise amplifier.

When atoms are bound together in a metal or crystal, their electrons become bound to the material as a whole, and their energy levels cease to be precise. Instead, the electrons find themselves confined to energy bands; they are permitted to reside anywhere in the bands, but are forbidden to occupy energy states between them. Since the density of electrons in an energy band is limited by the Pauli exclusion principle, once a particular band is filled, any additional electrons must occupy a state in the next-higher band.

Metals are conductors because their highest energy band is only partially filled. Thus, when an electrical potential is placed across a sample, the electrons jump to higher energies within the same band and create a current by flowing down the potential. For insulators, however, all of the energy bands with electrons are filled, and no current is produced by an applied potential drop because the electrons are not permitted to change their energy and move down the potential, unless they acquire sufficient energy to jump to a higher band which contains no electrons.

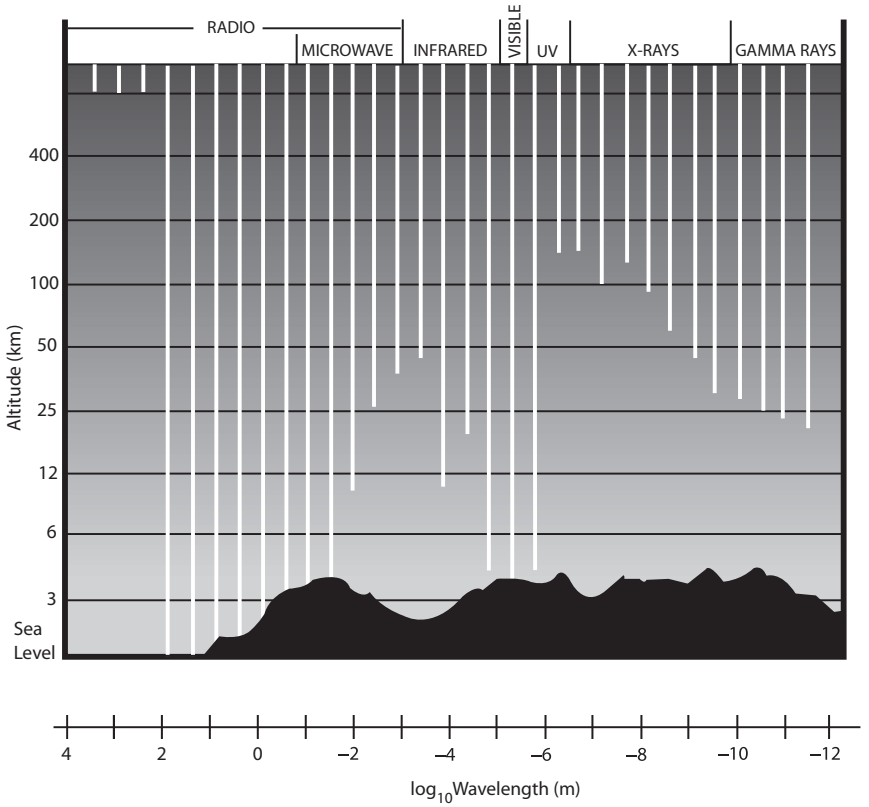

Figure 1.4 Transparency of Earth's atmosphere as a function of wavelength, showing the depth (in km) to which photons of a given energy will penetrate before being absorbed or scattered. The surface of the Earth is completely shielded from that portion of the spectrum (beyond the UV) of particular relevance to high-energy astrophysics. (Image courtesy of Jerry Woodfill and NASA)

The electrons in a CCD absorb UV photons or X-rays and jump to a higher energy band (leaving an electron "hole" behind), where they are collected and counted. The number of electrons is proportional to the X-radiation absorbed by the pixels (see figure 1.5). Depending on the type of material used in the detector elements, the energy required to produce an electron–hole pair is only a few eV (e.g., 3.5 eV per pair in silicon and 2.94 eV per pair in germanium), so these detectors are ideally suited to UV observations.

CCDs such as this have allowed astronomers to study one of the least explored windows of the electromagnetic spectrum—the extreme UV (EUV). Until recently, astronomers thought that the mixture of hydrogen gas and other less abundant gases filling the interstellar medium would absorb virtually all EUV radiation before reaching Earth. This region of the spectrum therefore became known as the "unobservable ultraviolet." But the high quantum efficiency of these devices has facilitated the detection of very faint objects. For example, later in this book, we will learn

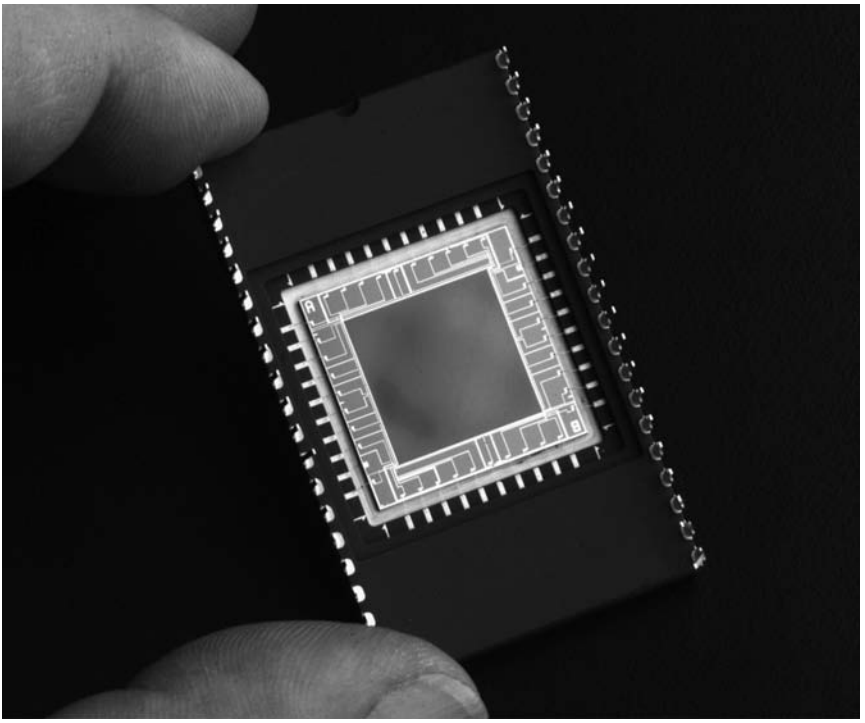

Figure 1.5 Photograph of a specially developed charge-coupled device (CCD) for use in ultraviolet imaging. A CCD is a sensor consisting of an integrated circuit containing an array of coupled capacitors (i.e., pixels). Typically several cm in size, each such detector contains thousands of pixels no bigger than $\sim$15 μm across. A UV or soft X-ray photon entering one of these pixels liberates an electron, which remains trapped until an external circuit transfers the collected electric charge from one capacitor to the next, or to a receptor outside the CCD. Because of the high quantum efficiency of these devices, photons can be counted very accurately, allowing even very faint objects to be observed. (Image courtesy of the Imaging Technology Laboratory at the University of Arizona)

about Cataclysmic variables—binary star systems in which the mass of one star is transferred to a white dwarf accretor, causing dramatic changes in EUV brightness.

The idea of the incident photon knocking out an electron within the detector is central to most high-energy devices, though the actual structure of the instrument depends on whether the dominant electron–photon interaction is photoelectric, Compton scattering, or pair creation. In our discussion of Earth's atmosphere, we already introduced the idea that the photoelectric effect dominates at energies $\epsilon \lesssim$ 60–80 keV, the X-ray and soft γ-ray portion of the spectrum. During the pioneering days of high-energy astronomy, a commonly used device for X-rays ($\epsilon \lesssim 20$ keV) was the proportional counter, basically a gas-filled discharge tube with a voltage drop across the gas. An X-ray photon entering the tube produced a high-energy electron, which then initiated a cascade of electron–ion pairs as it accelerated across the tube. In these devices, the current pulse measured by the counter was proportional to the

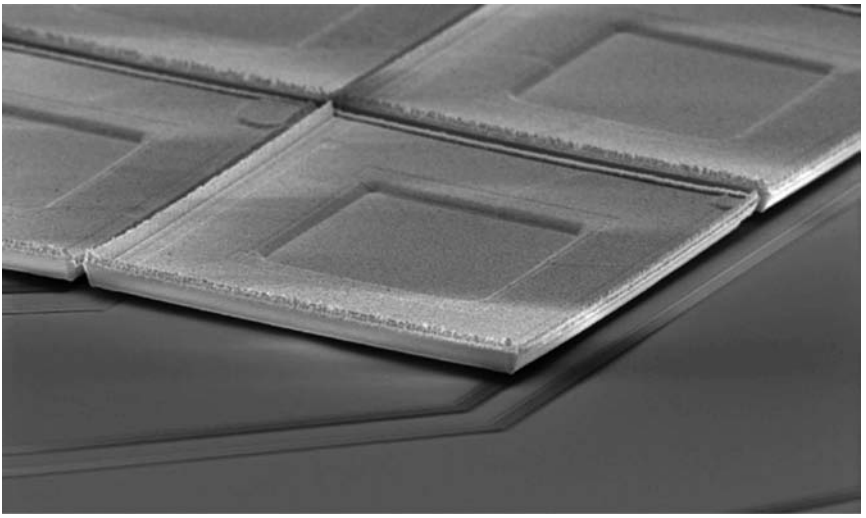

Figure 1.6 A microcalorimeter is a small device for measuring energy absorbed in the form of heat. It consists of an absorber, coupled thermally to a constant-temperature heat sink and to a thermometer that can measure changes in its temperature. The energy of an absorbed X-ray photon is dissipated into heat, causing a minuscule change in temperature. The photon's incoming energy is proportional to this change. Shown here is a scanning electron microscope image of 240-μm cantilevered Bi/Cu X-ray absorbers on a fully integrated array. The imaging spectrometer on the Constellation-X incorporates a 32×32-microcalorimeter array, and has high quantum efficiency, with 4-eV resolution near 6 keV, 2-eV resolution near 1 keV, and the ability to count at rates of up to 1000 events per second per pixel. (Image courtesy of NASA)

deposited energy, which then yielded the information necessary to reconstruct the X-ray spectrum.

Unfortunately, during this era the choice between wavelength dispersive devices (such as Bragg crystals or grazing incidence diffraction gratings) and nondispersive spectrometers (solid-state detectors or proportional counters) presented somewhat of a dilemma. Dispersive spectrometers offered very good energy resolution, but only at low throughput (the rate at which photons can enter the device and are detected). Nondispersive spectrometers, on the other hand, had very high efficiency, but relatively poor resolution.

Today, the detector of choice for X-ray instrumentation is the microcalorimeter, which provides several advantages over these older methods (see figure 1.6). The energy deposited by the incoming high-energy photon is measured after it has been converted into heat, without the need to worry about the charge transport properties of the absorber. Calorimeters can therefore incorporate a wide variety of materials.[11]

[11] The first microcalorimeters for X-ray astronomy were developed by the University of Wisconsin and the NASA Goddard Space Flight Center. They were first employed on a sounding-rocket experiment (the X-ray quantum calorimeter XQC) launched in late 1995. This device had an array of microcalorimeters to study the X-ray background in the energy range 30–1000 eV.

A cryogenic microcalorimeter is composed of three parts, an absorber, a sensor that detects temperature variation in the absorber, and a weak thermal link between the detector and a heat sink. When an X-ray photon hits the absorber, its energy is eventually converted into thermal phonons and the temperature of the detector first rises and then returns to its original value set by the weak thermal link to the heat sink. This detector is also a type of proportional counter, in that the temperature change is proportional to the energy of the incident X-ray. The sensor is a resistor whose resistance is a strong function of temperature. The requirements for a good microcalorimeter are therefore an absorber with a small heat capacity able to convert the incident radiation into thermal phonons quickly and with high efficiency, and a sensor with low heat capacity and high sensitivity to temperature variations.

The development of microcalorimeters has been so promising that the Constellation-X Observatory, a key mission in NASA's Beyond Einstein Program, will feature microcalorimeters in its detection infrastructure. This mission will be a combination of several X-ray telescopes flying in unison to generate the equivalent observing power of one giant telescope, with a projected launch date of 2016. The combination of four telescopes in the array will provide a sensitivity 100 times greater than any other X-ray instrument ever flown. To meet the design requirements of efficiency and spectral resolution, Constellation-X will employ the X-ray microcalorimeter spectrometer, consisting of a 32×32 array of microcalorimeters with superconducting transition-edge sensor thermometers (see figure 1.6). One of the most challenging aspects of this design will be to meet the cooling power necessary to reduce the ambient temperature in the device to $\sim$50 mK.

All X-ray telescopes, including Constellation-X (see section 1.5), must also be able to focus X-rays onto the detector. Unlike optical photons, X-rays reflect from the surface of conducting materials only at large angles of incidence i. For example, at energies $\epsilon \sim 1$ keV, reflection occurs for $i \gtrsim 87°$, and i increases rapidly toward 90° with increasing photon energy. X-ray telescopes must therefore incorporate a mirror assembly shaped like nested "barrels" (see figure 1.7), in which incoming photons approach along essentially parallel paths from great distances and reflect at grazing angles off a combination of hyperbolic and parabolic metallic surfaces to arrive at a focal point several meters beyond the telescope's front end. This type of structure therefore produces telescopes with relatively long focal lengths, as one can see with a quick inspection of plates 1 and 2, showing artists' views of two recently flown X-ray observatories (*Chandra* and XMM-*Newton*).

The efficiency of X-ray detectors drops off quickly above $\sim$20 keV, either because the ionizing cross section depends strongly on the incoming photon's energy ($\sim\epsilon^{-3}$), or because photons become progressively more penetrative and difficult to capture by the microcalorimeter pixels. For energies between $\sim$20 keV and several MeV, the most common device for detecting radiation is the scintillation counter.

The basic element of this technique is a crystal (such as CsI or NaI) in which the entering γ-ray Compton scatters several times before photoelectric absorption occurs. At these energies, the scattering is inelastic, and the photon loses energy with each interaction. The crystal subsequently converts the ionization energy lost by the excited electrons and crystal atoms into visible light, which in turn is converted into an electrical signal by a photomultiplier tube. It is important to stress that

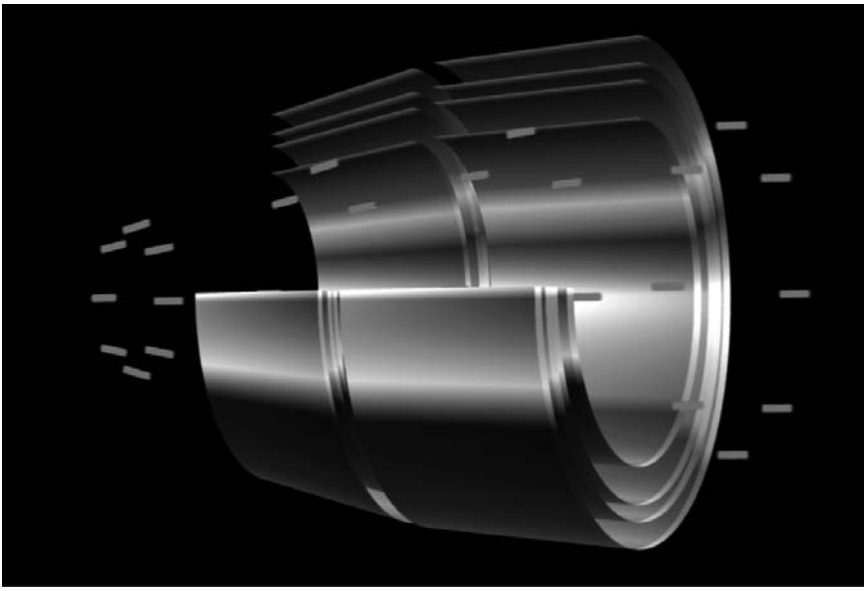

Figure 1.7 Unlike visible light, which reflects off mirrors at all angles of incidence, X-rays have such high energy that they penetrate (and get absorbed) below the surface of the reflector, unless they strike at grazing angles. X-ray telescope mirrors must therefore be shaped like "barrels" to reflect the incoming photons (from right to left in the image) and focus them to a point at the detector. Fortunately, this configuration allows many such mirrors (tens or more) to be nested together about the common symmetry axis, thereby greatly enhancing the flux of X-ray photons that may be brought to a focus. (Image courtesy of NASA/CXC/SAO)

because of the multiple Compton scatterings, it is difficult to use the excited electrons within the crystal to indicate directionality. As such, a hard X-ray/soft γ-ray detector utilizing this technology must rely on other telescope components (e.g., a coded mask aperture, as illustrated in figure 1.10) to provide information on the incoming photon's trajectory.

In the 1990s, one of the major instruments aboard the *Compton* Gamma Ray Observatory (GRO), known as COMPTEL, was a standout example of how successful this technique can be. COMPTEL consisted of two detector arrays, as shown in figure 1.8. A liquid scintillator, NE 213A, was used in the upper one, and NaI crystals appeared in the lower. Incoming γ-rays were detected by two successive interactions: the first was a Compton scattering event in the upper detector; the second was total absorption in the lower one. By measuring the locations of the interactions and energy losses in both cases, one could then determine the energy and direction of the incoming photon.

As shown in figure 1.8, the two detector planes were separated by a distance of 1.5 m. The 7 cylindrical D1 modules in the upper plane were each 27.6 cm in diameter, 8.5 cm thick, and the whole assembly was surrounded by eight photomultiplier tubes. The total area of the upper detector was approximately 4188 cm^2. By comparison, the 14 D2 modules in the lower plane consisted of cylindrical NaI blocks,

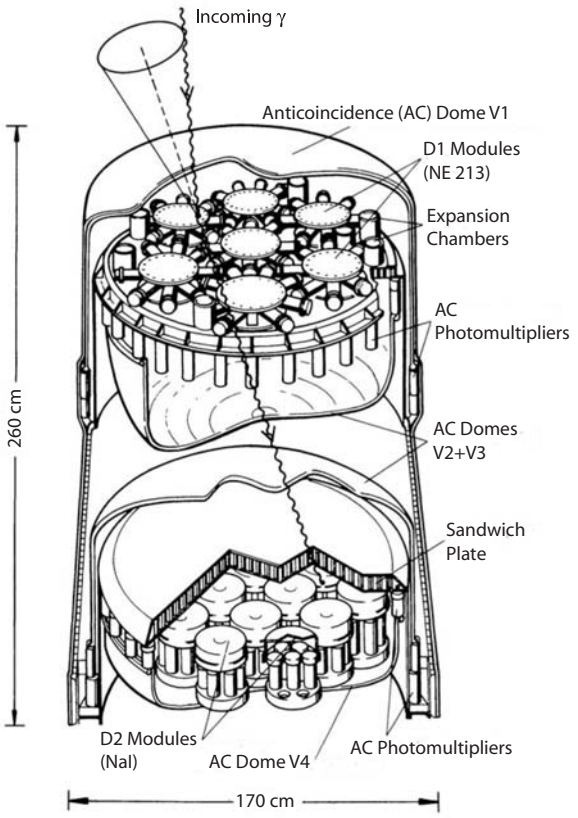

Figure 1.8 The Compton telescope approach to γ-ray detection, illustrated here for the particular implementation in the COMPTEL telescope on the *Compton*-GRO. (From Schoenfelder et al. 1993)

each 7.5 cm thick and 28 cm in diameter. Each block of NaI was viewed from below by seven photomultiplier tubes. The total geometrical area of the lower detector was 8620 cm^2.

As one can imagine, a chief source of error in measuring the incoming photon's energy is the possible loss of information along the sequence of interactions within the detector assembly. The photon's energy is estimated by summing the energies deposited in the upper and lower detectors, assuming total absorption of the scattered photon. Then, from the energy losses and the interaction locations, one determines the arrival direction of the incoming γ-ray. In practice, one must also fold into the analysis a detailed understanding of the properties of the scintillation detectors, and of the response of the telescope to background, multiple interactions, and partial absorption events, to arrive at a final determination of the photon's energy and direction of flight. A cutaway image of the COMPTEL telescope is shown in figure 1.9.

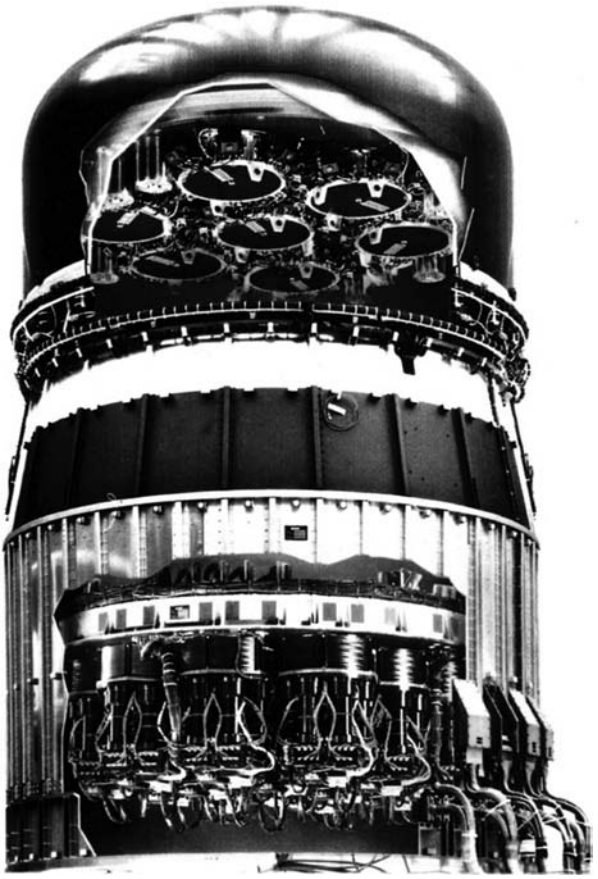

Figure 1.9 A cutaway image of the COMPTEL telescope on the *Compton-GRO*. COMPTEL consists of two detector arrays. A liquid scintillator, NE 213A, is used in the upper seven cylindrical modules, each of which is 27.6 cm in diameter, 8.5 cm thick, and viewed by eight photomultiplier tubes. In the lower array, 14 cylindrical blocks of 7.5 cm thickness and 28 cm diameter contain NaI crystals, each of which is viewed from below by seven photomultiplier tubes. The two detectors are separated by 1.5 m, and each is surrounded by a thin anticoincidence shield of plastic scintillator that rejects charged particles. The incoming γ-rays are detected by two successive interactions: an incident photon is first Compton scattered in the upper detector and is then totally absorbed in the lower one. The interaction sites are measured and the energy losses are determined. The overall energy and angular resolution of the telescope depends on the accuracy of these measurements. (Image courtesy of COMPTEL/NASA)

Today's hard X-ray/soft γ-ray detector designs often call for the inclusion of another component to help with directionality. The most common approach is the so-called coded aperture imaging to localize the incident photons. A coded aperture is a mask (see figure 1.10) positioned in front of the actual γ-ray detectors. The coded mask aperture sits about one meter above the detector plane and is made from $\sim$50,000 lead tiles arranged in a random half-open/half-closed pattern. Each tile

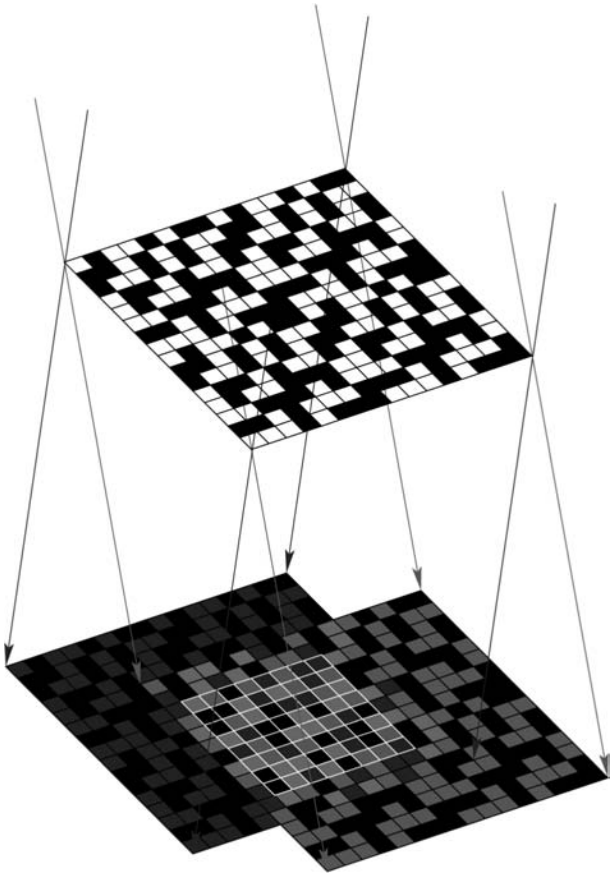

Figure 1.10 Since radiation above ∼20 keV cannot be focused with current technology, present day high-energy detectors use a technique known as coded aperture imaging, in which an absorbing mask (such as lead) is positioned in front of the position-sensitive γ-ray detector. The lead tiles are arranged in a random half-open/half-closed pattern. Some of the incoming γ-rays are stopped by the mask; others pass on through to the detectors. Analysis of the resulting shadow determines the direction of incoming photons. If more than one source exists in the field of view, one may find the direction to each source by finding the multiple shadows cast on the detector plane. Several-arcminute spatial resolution is feasible with this technique. (Image courtesy of IBIS/INTEGRAL and ESA)

might be as small as $5 \times 5 \times 1$ mm^3. The idea behind this approach is that the lead tiles stop some incoming photons, while the apertures let in the rest. In so doing, the mask casts a shadow on the detector plane, and using the measured position of this shadow, and the known locations of the lead tiles, one can then determine the direction of the γ-ray source.

The coded mask aperture yields a less precise determination of the incoming photon's direction than X-ray mirrors do (see figure 1.7), but at energies beyond ∼20 keV there is currently no better choice. Note that when more than one source is

present in the field of view, one can still find the direction to each object by finding the multiple shadows cast on the detector. Telescopes designed on this principle can locate a source with an accuracy of several arcminutes. This method only works for locating point sources, however; diffuse emission cannot be imaged with this technique.

At energies $\epsilon \gtrsim 3\,\mathrm{MeV}$, photons become energetic enough to create electron–positron pairs, as we learned in our earlier discussion on atmospheric absorption. This interaction takes place within the CsI or NaI crystal, and one can, in principle, also use the direction of motion of the leptons (which tend to move in a forward direction relative to the incoming γ-ray) to infer the photon's angle of incidence into the detector.

But there's a limit to how far up in energy we can go with this technique because very high-energy γ-rays do not stop with the creation of just one pair of leptons; they produce cascades of particles and secondary radiation that cannot all be trapped within the detector. In this domain, the atmosphere actually becomes a help rather than a hindrance, because incoming photons strike the mesosphere, some 30–100 km above Earth's surface, and produce a glow of light detectable with air Cerenkov detectors on the ground (see figure 1.11). Of course, this process occurs for many different types of energetic particles entering the atmosphere, though our principal interest here is γ-rays.

This technology has evolved significantly since the early days. In the late 1920s, the French scientist Pierre Auger discovered the phenomenon of extensive air showers using ionization chambers, Geiger counters, and cloud chambers. He determined that very energetic cosmic rays (including γ-rays) could produce showers of secondary particles that spread out over several hundred meters. Atmospheric fluorescence was incorporated into the detector design of the 1980s, using the idea that charged particles passing by molecules in the atmosphere transfer some of their energy to the target particles. This has the effect of "shaking up" the electrons inside the molecules, thereby emitting secondary (or fluorescent) radiation as the electrons return to their normal configuration. Nitrogen molecules, the main constituents of air, produce blue fluorescent light, which can be sensed by photomultipliers on the ground. But this light is so faint that it can be seen only on moonless nights without clouds. This technique has successfully been used by several facilities, including the Fly's Eye experiment in Utah and, most recently, the Pierre Auger Observatory in Argentina.

The cascade of particles produced by the incident γ-ray (or, more generally, by the incident cosmic ray) also produces a glow of radiation by another mechanism, known as the Cerenkov effect. The speed of light in transparent materials is less than its value in vacuum ($c = 3 \times 10^{10}\,\mathrm{cm\ s^{-1}}$). In water, for example, light travels at $0.7c$. Particles with mass, however, can travel at speeds greater than this, creating a shock front of light that spreads out in a cone around the particle. Photomultiplier tubes placed within this medium sense the Cerenkov light, and one can then use the intensity and pattern of this radiation to infer the energy of the incident high-energy γ-ray. The use of several optical telescopes on the ground can even provide information on the source direction (to within a degree or so) with reconstruction of the various images.

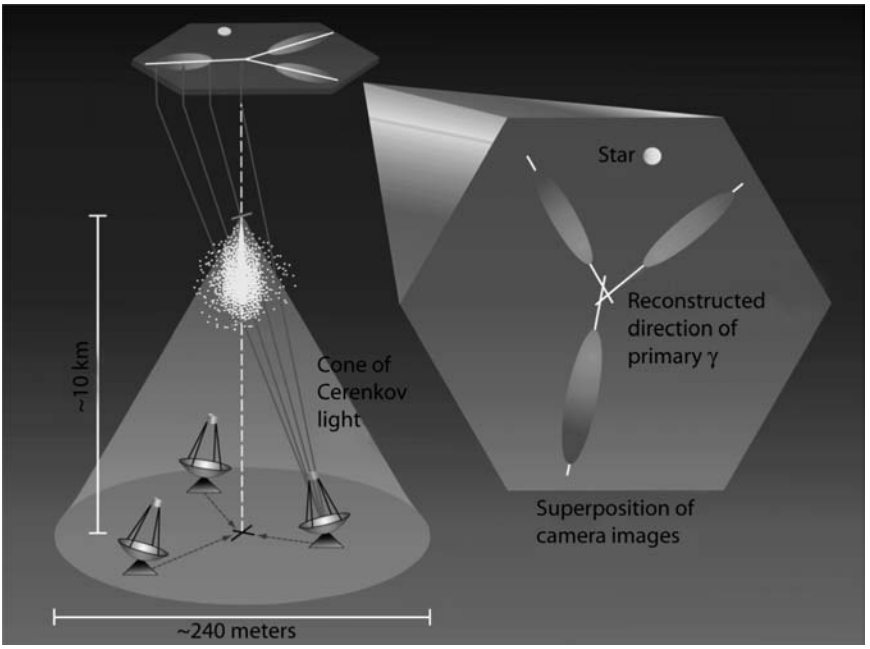

Figure 1.11 An energetic particle passing through Earth's atmosphere transfers its energy to charges at an impact point tens of kilometers above the ground. The cascade ensuing from this process includes particles moving through the medium at speeds greater than the speed of light in that region, producing a shock front of light, known as Cerenkov radiation, spreading out in a cone toward the ground. One or more Earth-based telescopes image this light, providing a measure of the incoming cosmic ray's direction and energy. (Image from Clery 2004. Illustration by K. Buckheit. Reprinted with permission from AAAS)

1.5 HIGH-ENERGY TELESCOPES

The development of high-energy astrophysics as an observational science has been so rapid since the rocket experiments of the early 1960s that it is no longer possible to list all of the missions within a reasonably limited space. The best we can do now is to catalog the principal missions since 1990, and to highlight the capabilities and scientific motivation for some of the more prominent satellites. But though the vast majority of high-energy astrophysics experiments have been conducted in space, we should not forget that observations may also be carried out at high altitudes within Earth's atmosphere, and we begin with a "status" report of where things stand with regard to NASA's ballooning program.

High-altitude balloons have for many years offered the capability of inexpensively lofting high-energy instruments to altitudes of 30 km or more (above most of Earth's atmosphere) for long-duration flights lasting several months (see figure 1.12). While the basics of ballooning remain unchanged over time, the balloons themselves have increased in size, and have become more reliable with each succeeding generation.

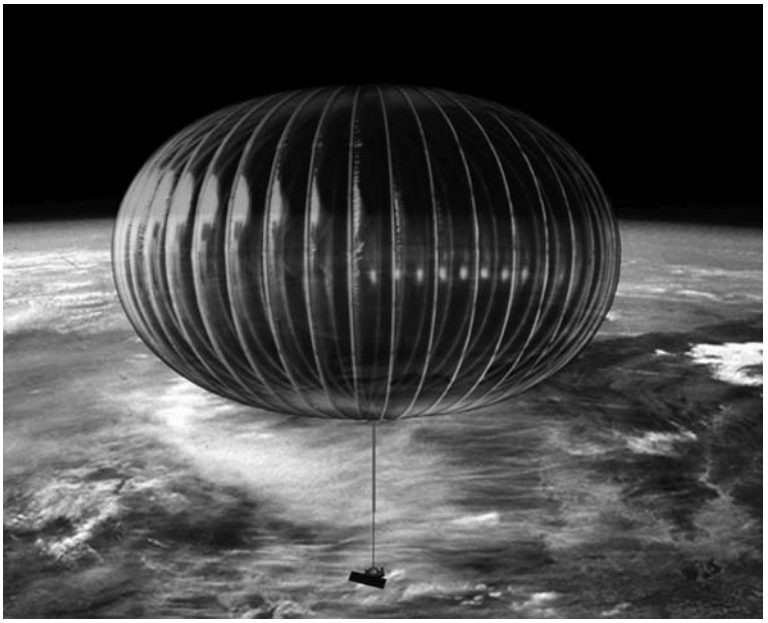

Figure 1.12 An artist's concept of NASA's Ultra Long Duration Balloon (ULDB), a structure composed of a lightweight polyethylene film about the thickness of ordinary plastic food wrap. Designed to lift 6000 pounds, it can rise to an altitude of about 33 km above 99% of Earth's atmosphere, for durations approaching 100 days. (Image courtesy of NASA)

The Goddard Space Flight Center's Wallops Flight Facility, which manages the Balloon Program, launches missions from permanent launch sites in Palestine, Texas, and Ft. Sumner, New Mexico, and from remote sites in the United States, Canada, Australia, New Zealand, and Antarctica.

NASA's balloons are made of a thin polyethylene material with a thickness like that of an ordinary sandwich wrap. When fully inflated, these balloons range up to 200 m in diameter and are taller than a 60-story building. The complete facility includes the balloon, a parachute, and the instruments themselves. Given their enormous size, these structures have a powerful lift, and can carry a payload with the weight of three small cars.

One of the most notable successes of this program was the balloon mission in 1998, named the Balloon Observations of Millimetric Extragalactic Radiation and Geophysics experiment (more commonly known as BOOMERANG), which returned what were then the highest-ever-resolution images of the cosmic microwave background. Perhaps just as important, all of the devices that flew on the Cosmic Background Explorer (COBE), the pioneering satellite that revealed fluctuations in the background radiation in the early 1990s, had been flight-tested on earlier balloon experiments.

In fact, the ballooning program continues to serve this very useful purpose of flight testing exploratory (or new concept) instrumentation for possible use in future orbital missions. It also provides the capability for carrying out small-scale missions

that would not be feasible with a full launch into space. For example, in late 2006, the Wallops Facility launched the High Altitude Student Platform, carrying science experiments developed by student groups from across the United States, to an altitude of approximately 40 km for a total flight time of about 18 h. The scientific goals included the study of the cosmic ray flux, tests of various rocket nozzle designs, tests of an accelerometer based inertial guidance system, and remote sensing imaging.

In space-based X-ray astronomy, the first Earth-orbiting explorers were launched in the early 1970s (*Uhuru*, SAS-3, and Ariel-5), followed later in that decade by larger missions, such as HEAO-1, *Einstein*, EXOSAT, and Ginga. Their success, particularly in providing the first X-ray images of the sky (discussed at greater length in chapter 2), moved X-ray astronomy into the mainstream of scientific research. In the 1990s (see figure 1.13), the US–European ROSAT survey detected over 100,000 X-ray objects, the Japanese ASCA mission obtained the first detailed X-ray spectra of these sources, and the *Rossi*-X-ray Timing Explorer (RXTE) studied their timing behavior. Near the end of this decade, the launch of the *Chandra* and XMM-*Newton* observatories introduced high-resolution imaging and a high-throughput capability to our repertoire.

Gamma-ray astronomy has also advanced significantly since the middle of the 20th century, first with the Small Astronomy Satellite 2 (SAS-2) and Cos-B in the early 1970s, which made the first surveys of the γ-ray sky, and then most impressively with the *Compton* Gamma Ray Observatory in 1990, and more recently with the US–European INTEGRAL mission in 2002. But one cannot fail to notice that the number of γ-ray missions is significantly lower than their X-ray counterparts. As we noted earlier in this chapter, very high-energy photons are more difficult to corral and measure, so progress in improving spatial and energy resolution is slower the higher the energy of the radiation. For this reason, new γ-ray missions enter the pipeline more slowly than experiments in the UV and X-ray domain.

In the remainder of this chapter, we describe a handful of the principal missions featured in figure 1.13, not to exclude the rest, but simply to provide an overview of the various capabilities required for a comprehensive high-energy astrophysics program. The very beginning of the 1990s saw the successful launch and deployment of the Roentgen Satellite (ROSAT), a German–US–UK collaboration. This mission lasted almost 9 yrs and produced, within the first 6 months of operation, one of the most dramatic all-sky surveys ever made. (We will see a sample image from this survey in plate 5.)

By way of comparison, ROSAT's sensitivity was about a factor 1000 better than that of *Uhuru*, the first Earth-orbiting explorer. ROSAT's energy coverage was 0.1–2.5 keV in X-rays, and 62–206 eV in the Extreme UV (EUV). One of the principal instruments aboard the satellite was a pair of position-sensitive proportional counters (based on technology that preceded the microcalorimeter development discussed in section 1.4) with an energy resolution $\Delta E/E \sim 0.5$. A second instrument was the High Resolution Imager (HRI) with a spatial resolution of $\sim 2''$. The scientific return from this mission was enormous, encompassing not only the highly detailed all-sky surveys at X-ray and EUV energies, but also extensive pointed observations of supernova remnants and clusters of galaxies, studies of unusual objects such as

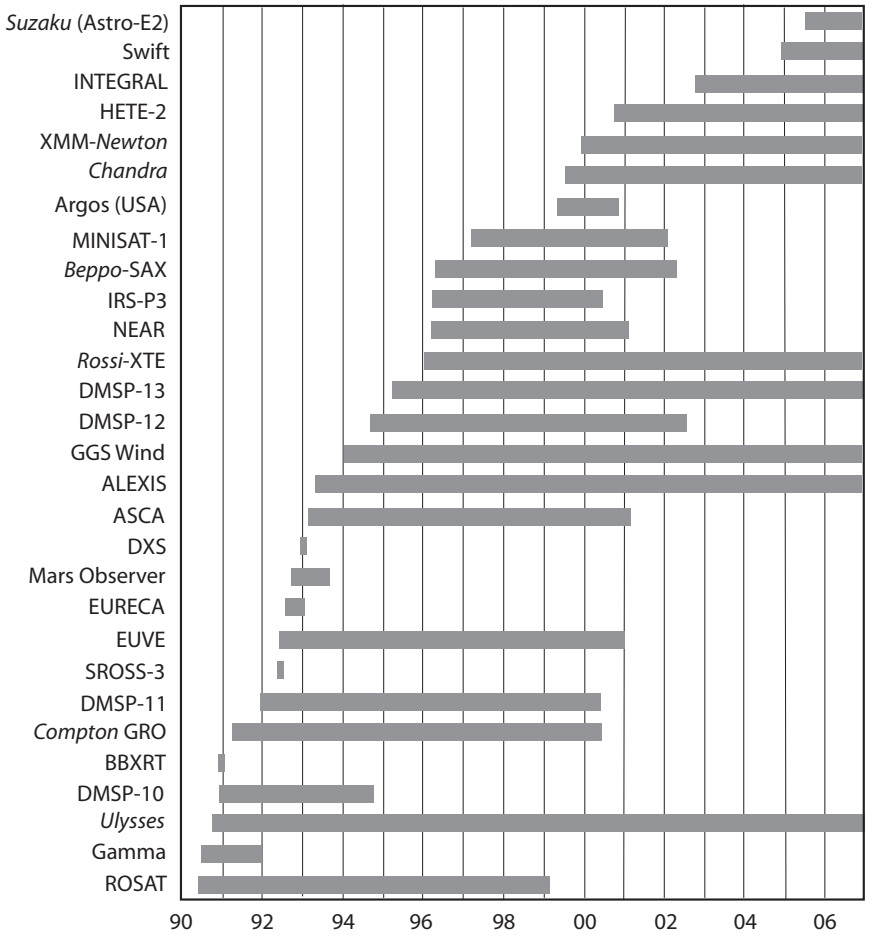

Figure 1.13 Timeline of principal high-energy astrophysics missions since 1990.

Geminga (for which X-ray pulsations were finally detected), and the discovery and observation of isolated neutron stars.

The *Compton* Gamma Ray Observatory (CGRO) was launched the following year and made breathtaking discoveries in the γ-ray sky until its gyroscopes began to fail, forcing NASA to bring it down from orbit in June 2000. Unlike most other satellites, CGRO was too big (about the size of a school bus) to burn up entirely during reentry in the atmosphere and so its descent had to be controlled by NASA, forcing a termination to what would otherwise have been a longer mission. The second of NASA's great observatories, CGRO had four instruments covering six orders of magnitude in energy, from 30 keV to 30 GeV. Its payload included the Burst and Transient Source Experiment (BATSE), an all-sky monitor covering the energy range 30 keV to 1 MeV, whose main role was to study the mysterious nature of γ-ray bursts (GRBs). Among its many exciting discoveries, BATSE produced the catalog of

GRBs shown in plate 8, demonstrating without any lingering doubt that these events must occur at cosmological distances, given their isotropic distribution in the sky.

The second instrument aboard CGRO was the Oriented Scintillation Spectrometer Experiment (OSSE), covering the energy range 50 keV to 10 MeV, which produced, among other things, a map of the Milky Way in the ^{26}Al γ-ray line. The third detector was the Compton Telescope (COMPTEL), capable of $\sim$1-steradian imaging in the energy range 0.8–30 MeV. This facility was featured earlier in figures 1.8 and 1.9, and the all-sky survey it produced is shown in plate 8. The fourth (and final) instrument on CGRO was the Energetic Gamma Ray Experiment Telescope (EGRET), spanning the range 30 MeV to 30 GeV. EGRET discovered the powerful γ-ray luminosity of superluminal AGNs, and produced the all-sky survey shown in plate 11.

The *Rossi* X-ray Timing Explorer (RXTE) broke new ground by being the first major mission designed for timing studies, as opposed to pure imaging or spectral measurements. Launched in December 1995, RXTE is capable of only moderate spectral resolution, but can discern source variability on timescales of months down to microseconds, covered in a broad spectral range from 2 to 250 keV. As discussed in section 1.2, this coverage in timing resolution is sufficient to detect even the highly dynamic variability on the surface of a neutron star. Its strength is the very large collecting area—6500 cm^2 for its proportional counter array (PCA), and 1600 cm^2 on the High-Energy X-ray Timing Experiment—which accumulates good photon statistics quickly to allow for fine temporal resolution. Among its scientific achievements, RXTE discovered kilohertz quasi-periodic oscillations (QPOs) in compact binaries (see section 10.4), X-ray afterglows in some GRBs, state transitions in the black-hole binary Cygnus X-1, and accretion instabilities in accreting neutron-star systems.

As we approach the current era in figure 1.13, we encounter one of the finest high-energy missions ever flown. The *Chandra* X-ray Telescope (shown schematically in plate 1) has made some truly unprecedented observations in the energy range 0.1–10 keV. With its unmatched $\sim 0.''5$ angular resolution, eight times better than any other X-ray telescope ever flown, *Chandra* has provided us with detailed images of the full impact of supernova blast waves, brown-dwarf flares, the cannibalization of one small galaxy by another, and the rich high-energy phenomena pervading the central region of our Galaxy. We will be featuring observations made with *Chandra* throughout this book, including the Deep Field view of the X-ray cosmos in plate 6, and the highly detailed view of the galactic center in plates 20 and 21.

Launched in July 1999, *Chandra* became the third in NASA's family of great observatories, following the *Hubble* Space Telescope and the *Compton* Gamma Ray Observatory. One of its greatest contributions to X-ray astronomy has been the resolution of the X-ray background, made possible not only because of *Chandra's* resolution, but also by its sensitivity to detect sources more than 20 times fainter than before.

XMM-*Newton* is a contemporary of *Chandra*, and is suitably designed to complement the latter's capabilities (see plate 2). The European Space Agency's (ESA) X-ray Multi-Mirror Mission was launched by Ariane 504 in December 1999, the second cornerstone satellite in ESA's Horizon 2000 Science Program. Whereas *Chandra's* imaging power is unmatched, XMM-*Newton's* strength is its unprecedented effective area ($\sim$1500 cm^2 for each of three co-aligned telescopes), which, together

with its orbit that permits long, uninterrupted exposures, provides high sensitivity for detecting faint sources with excellent spectral resolution (with $E/\Delta E$ as high as 200–800 between 0.35 and 2.5 keV on the Reflection Grating Spectrometer). This satellite also carries an optical monitor, the first ever flown on an X-ray observatory, permitting simultaneous X-ray and optical observations of the same source.

Two examples that highlight XMM-*Newton's* strengths are provided in figures 9.14 and 12.11. These illustrations span the range of source size, from a compact binary containing an accreting white dwarf in the former, to the supermassive black hole at the center of our Galaxy in the latter. The X-ray flare seen in figure 12.11 is particularly important because it is the first event ever to be compellingly associated with phenomena occurring just outside a supermassive black hole's event horizon. As we shall see in chapter 12, the quasi-periodic modulations in this lightcurve correspond to an emitter orbiting at $\sim$3 Schwarzschild radii, right around the marginally stable orbit where the accretion disk is thought to end before its material plummets toward oblivion.

The most recent X-ray mission, now known as *Suzaku*, was actually part of *Chandra* in its original design. More accurately, one should say that *Chandra* and *Suzaku* were both part of the same mission concept called the Advanced X-ray Astrophysics Facility (AXAF). This was to be a combination X-ray imager (which became *Chandra*) and spectrometer (now *Suzaku*). Such a comprehensive design became prohibitively expensive and unmanageable, forcing NASA to abandon the simultaneous mission idea. But Astro-E2 (*Suzaku's* previous appellation) survived thanks to the Japanese Institute of Space and Astronautical Science (ISAS), which continued its development with US participation. *Suzaku* was launched in July 2005 from the Uchinoura Space Center in Japan, the first ever orbital mission to carry an X-ray microcalorimeter (see figure 1.6) for unparalleled energy resolution: at 6 keV, the X-ray Imaging Spectrometer (XRS) aboard *Suzaku* was designed to achieve an energy resolution of $\sim$6.5 eV. Sadly, the XRS failed shortly after launch and its potential scientific return has been lost to the mission. But having survived and operated flawlessly for 3 weeks after the satellite was deployed, the XRS has proven the point that this microcalorimeter technology can indeed work in space, and its promise will eventually be realized as new flight opportunities (e.g., with Constellation-X) become available.

The last two missions we will feature here are both γ-ray experiments, one already in orbit, the other to be launched in the very near future. The International Gamma-ray Astrophysics Laboratory (INTEGRAL) was launched into orbit by ESA in October, 2002 (see plate 3). Lifted into space on a Russian Proton rocket from Baikonur in Kazakhstan, INTEGRAL now revolves on a 72-hour elliptical orbit, ranging from 9000 km up to 155,000 km above Earth's surface. As the successor to CGRO, it is producing the next generation map of the sky in soft γ-rays, and is capable of performing high spectral and spatial observations of point sources. An example of what can be done with it is shown in figure 13.3, featuring the electron–positron annihilation-line distribution at the galactic center. Its energy coverage (3 keV to 10 MeV) is provided by a complement of several instruments, including the SPI spectrometer and the IBIS imager, both of which utilize a coded mask aperture for directionality (see figure 1.10).

As we look to the future, two principal high-energy missions loom on the horizon: Constellation-X, which we have already discussed in connection with the microcalorimeter technology, and the Gamma-ray Large Area Space Telescope (GLAST) (see plate 4). The former is in the pipeline for launch around 2016; the latter will be in orbit by the end of 2007. GLAST is the next generation high-energy γ-ray observatory designed for making observations of celestial sources in the energy band extending from 10 MeV to 100 GeV. Though it shares many features in common with EGRET on CGRO, its capabilities extend γ-ray astronomy well beyond what was achieved in the 1990s. Its detector is made of segmented 20-cm CsI bars, arranged to give both longitudinal and transverse information about the energy deposition pattern once a γ-ray comes in and causes a scintillation reaction. These bars function as small calorimeters and the light flash is photoelectrically converted into a voltage for readout.

The science mission of GLAST is rather ambitious, beginning with a one-year all-sky survey that will improve our view of the γ-ray sky from what we have now (courtesy of EGRET) in plate 11, to those simulated in plates 12 and 13. With a field of view ($\sim$2.5 steradians) about twice that of EGRET, and a sensitivity about 50 times greater at 100 MeV, its two-year limit for source detection is expected to be $\sim 1.6 \times 10^{-9}$ photons cm^{-2} s^{-1}, with a point-source positional accuracy of 30$''$ to 5 arcminutes. Its targets will include AGNs, whose jets are still poorly understood, the γ-ray background sky, which is currently blending the emission from the interstellar medium and a large number of as yet unidentified sources, GRBs, and possibly even sites of supersymmetric dark matter annihilation, which may produce monoenergetic γ-ray lines above 30 GeV.

The high-energy telescopes we have surveyed here only provide a brief overview of the general concepts. Looking back over the past 40 yrs, it is truly amazing to see how quickly technology has developed in this field, to the point where some missions are actually driving the development of instrumentation (e.g., microcalorimeter X-ray detection) that will find use in many other fields. Sadly, however, one cannot ignore a rather unsettling trend in figure 1.13: the second-order derivative of the launch times for these missions is negative. Rising costs and an ever-tightening budget in the United States are making it increasingly difficult to sustain a high-paced program. The growing participation by the European Space Agency, and countries such as Japan, however, is partially mitigating this effect. Let us all hope that high-energy astrophysics, a truly space-based science, continues to flourish in the decades to come and beyond.

SUGGESTED READING

A good collection of scholarly papers on the subject of archaeastronomy and the co-evolution of astronomy and culture may be found in the edited volume by Ruggles and Saunders (1993).

The beginning of high-energy astrophysics may rightly be traced to the earliest exploration for the source of ionization seen in laboratory experiments. An early paper on this topic was that by Hess (1912).

A complete history of high-energy astrophysics does not yet exist in book form. However, NASA's Goddard Space Flight Center has put together a reliable website attempting such a compilation, which the reader may find at http://heasarc.gsfc.nasa.gov/docs/heasarc/headates/heahistory.html.

X-ray astronomy began in 1962 with the first discovery of a high-energy source outside the solar system. Read about this observation in Giacconi et al. (1962).

In designing high-energy instruments, one must know the energy of the photons being detected, their flux, and how quickly the detection must be made in order to track the source variability. We have therefore included in this introductory chapter a brief discussion of a typical source luminosity and the associated dynamical timescale, even though we will not address the theory behind these concepts until later in the book. The reader will find a more complete presentation of issues dealing with radiative processes, including all the pertinent references, in chapter 5. In the meantime, it will also be useful to read chapter 1 in Rybicki and Lightman (1985).

In discussing the various interactions between incoming photons and Earth's atmosphere, we have limited our description to the essential results from quantum electrodynamics, without necessarily probing too far into the details. Many books on this subject now exist in the literature, but one of most insightful is still Landau and Lifshitz (1982).

To find a more detailed (and technical) description of the various detector technologies in high-energy astrophysics, the reader should consult articles in the proceedings of conferences on this topic. A good starting point is Siegmund and Flanagan (1999).

Throughout this book, but particularly in this chapter, we often refer to individual high-energy instruments and their capabilities. The National Aeronautics and Space Administration (NASA) in the United States, the European Space Agency (ESA) in Europe, and the Aerospace Exploration Agency (JAXA) in Japan, all maintain excellent instrument-specific websites, many of which continue to be updated as new data are collected and/or analyzed. The reader can find these at http://www.nasa.gov/missions/index.html, http://www.esa.int/esaSC/index.html, and http://www.jaxa.jp/index_e.html.